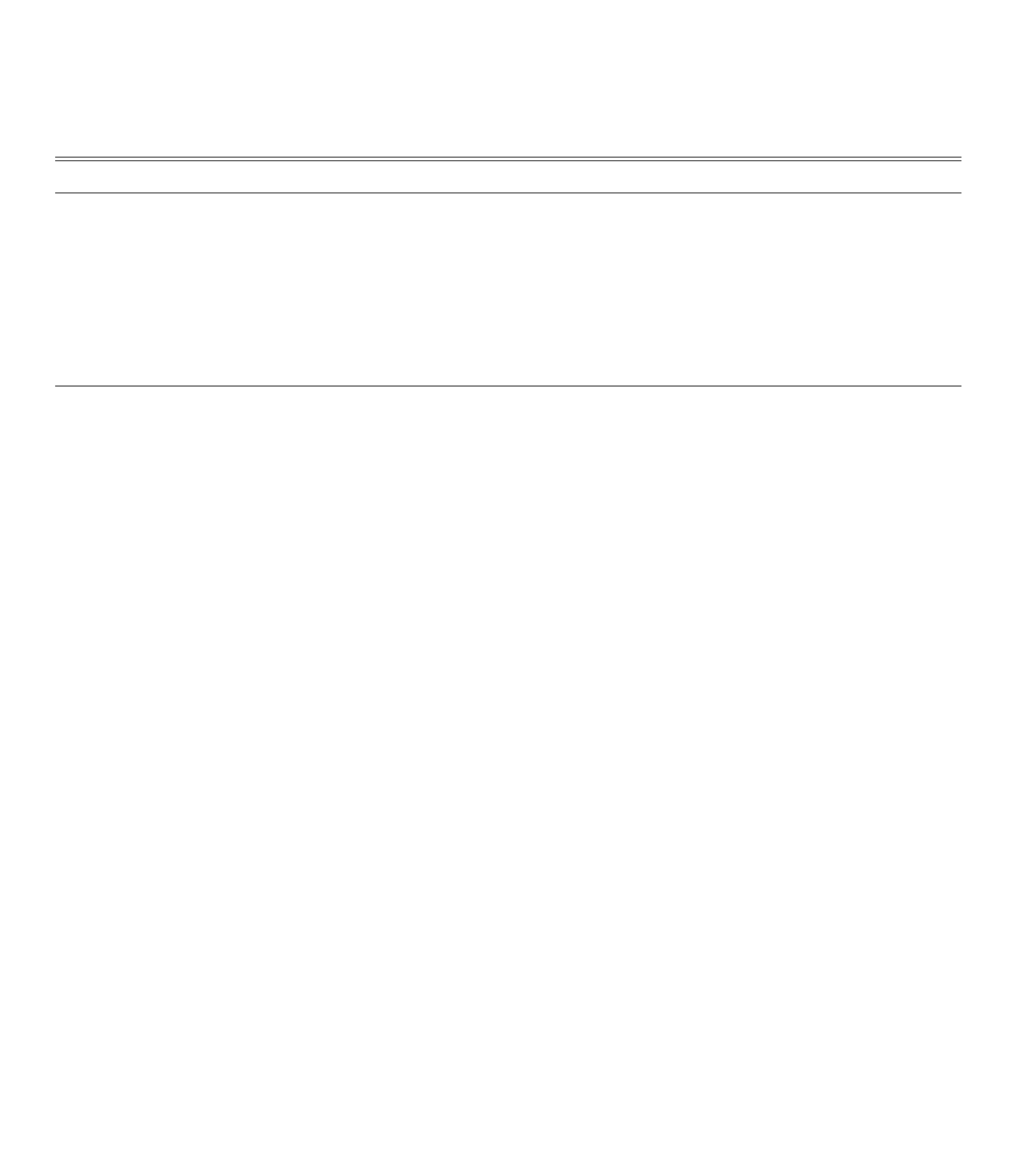


American Museum of Natural History, Department of Astrophysics, CPW at 79th, NY, 10024
Department of Earth and Space Science, Osaka University, Toyonaka, Osaka 560-0043, Japan
Astronomical Institute, Tohoku University, Sendai, Miyagi 980-8578, Japan
ALMA Project, National Astronomical Observatory of Japan, Mitaka, Tokyo 181-8588, Japan
CRAL, Ecole normale supérieure de Lyon, UMR CNRS 5574, France
School of Physics, University of Exeter, Exeter, EX4 4QL, UK

\_u \_\_ I \_<u>B</u> \_\_ \_\_ <u>J B B</u>

RAMSES

 $\underline{\hspace{1cm}}\phi$ 



In the original table, this dust-to-gas ratio was chosen so that the total surface-area of grains matches the uniform distribution of Kunz & Mouschovias (2009).

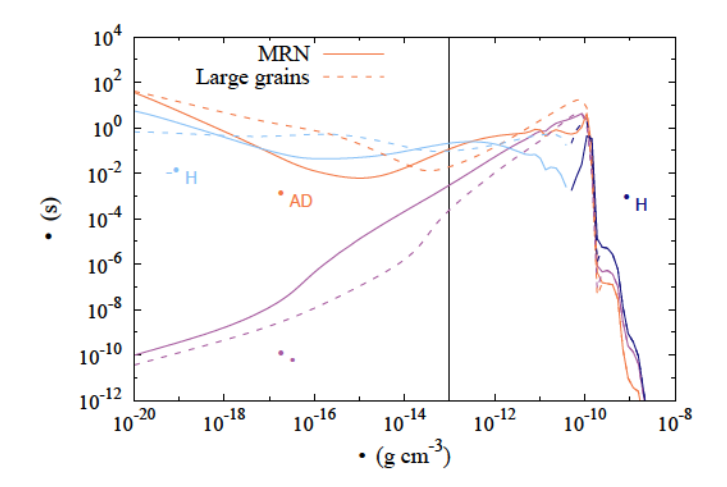


Figure 1. Non-ideal MHD resistivities as a function of density for the MRN distribution (solid lines), and the truncated distribution (dashed lines). Temperature scales with density according to equation 5, and, for this figure only, we assumed the following magnetic field prescription  $B=1.43\times 10^{-7}\sqrt{\rho/(\mu_{\rm P}m_{\rm H})}$  G (Li et al. 2011), with  $\mu_{\rm P}=2.31$  the mean molecular mass and  $m_{\rm H}=1.67\times 10^{-24}$  g the mass of one hydrogen atom. The vertical black line represents the first core formation density.  $\eta_{\rm H}$  represents the Hall resistivity, which can be negative.

also summarize the properties of the cores and the disks at  $t = t_{\rm C} + 4$  kyr.

We define the disk radius as the cylindrical radius containing 99% the disk's mass. Toomre's Q parameter is often used to quantify the stability of a disk against fragmentation, given by the following formula

$$Q = \frac{c_{\rm s}\Omega_{\rm d}}{\pi G \Sigma},\tag{9}$$

with  $c_{\rm s}$  the sound speed in the disk,  $\Omega_{\rm d}$  the disk average angular velocity and  $\Sigma$  the surface density of the disk. Q < 1 reflects an instability and a possible fragmentation. The AM is computed over the volume of the disk as

$$\mathbf{L}_{\text{disk}} = \int_{\text{disk}} \rho \mathbf{r} \times \mathbf{u} dV. \tag{10}$$

In this study, we always show the norm of the AM vector L, although its z-component is largely dominant.

Panel a of figures 4 and 5 shows that the disk mass evolution seems to be weakly dependent on the mass of the initial core and the grain size distribution. The low  $M_{\rm disk}$  and  $r_{\rm disk}$  of M2a4mrn in Table 2 are temporary and due to its fragmentation around this time-mark (see the dark red curve around 4 kyr in the panel a of Figure 5). The higher thermal support of  $\alpha=0.4$  simulations reduces the accretion rate, which yields a lower

disk mass. The radii of disks with the truncated distribution are overall larger for  $\alpha = 0.3$ , but only moderately for  $\alpha = 0.4$ . In the same manner, the Toomre's Q do not largely differ between the two grain models. The slightly larger value for the truncated MRN may be due to a self-regulation of spiral arms formed by gravitational instability, that transfer AM faster when they are more unstable. The difference is also clear when looking at the AM evolution. In the larger grains cases, the disks contain an amount of  $\sim 1-2 \times 10^{19} \text{ cm}^2 \text{ s}^{-1}$ more specific AM than their MRN cases counter-part, especially after 2.5 kyr, which is an increase of 10% to 20%. The trend is the same when looking at the normal AM. The Toomre's Q of all disks are lower than 1 after 2 kyr, which is reflected by the formation of large spiral arms ( $\sim 100$  au length). This low value is however not sufficient for the fragmentation of spiral arms, as was noted by Zhao et al. (2018). Takahashi et al. (2016) shows that the spiral arm fragmentation occurs when the local Toomre's Q in the arms becomes lower than 0.6. Therefore, the fragmentation of the disk can not happen as soon as Q < 1, but at later stages as it is the case in our simulations. The only run showing no fragmentation by  $t = t_{\rm C} + 4$  kyr is M2a4big, which is reflected by the largest Toomre's Q at  $t = t_{\rm C} + 4$  kyr. We observe that a larger  $\alpha$  provides smaller and less-massive disks with a lower AM. The Toomre's Q is larger and takes more time to reach values below 1. This behavior is mostly a consequence of the lower accretion rate due to the larger free-fall time.

To quantify the influence of the ambipolar diffusion in the disk, we calculate the Elsasser number, which is defined as

$$E_{AD} = \frac{4\pi u_A^2}{c^2 n_{AD} \Omega},\tag{11}$$

with  $u_{\rm A} = B/\sqrt{\rho}$  the Alfven speed, and  $\Omega$  the angular velocity of the fluid.  $E_{\rm AD}$  < 1 means that the ambipolar diffusion has a significant impact over the dynamics of the disk. Figure 6 displays the radial profiles of Am in the eight different disks, in which we have performed an azimuthal density-weighted average. Only the innermost 20 to 40 au parts of the disks show  $E_{AD} < 1$ , down to  $10^{-3}$ . In the outer regions,  $E_{AD}$  rises up to 10 to 100, indicating a less efficient decoupling between the magnetic field and the gas compared to the central domain. As a consequence of the higher ambipolar resistivity of the reference MRN distribution in the density range  $[10^{-14}:10^{-11}]$  g cm<sup>-3</sup>, the disks with the non-truncated MRN distribution have larger  $E_{AD} < 1$ regions than their truncated-MRN counter-part, up to a factor 2 for M2a3mrn and M2a3big. The truncated

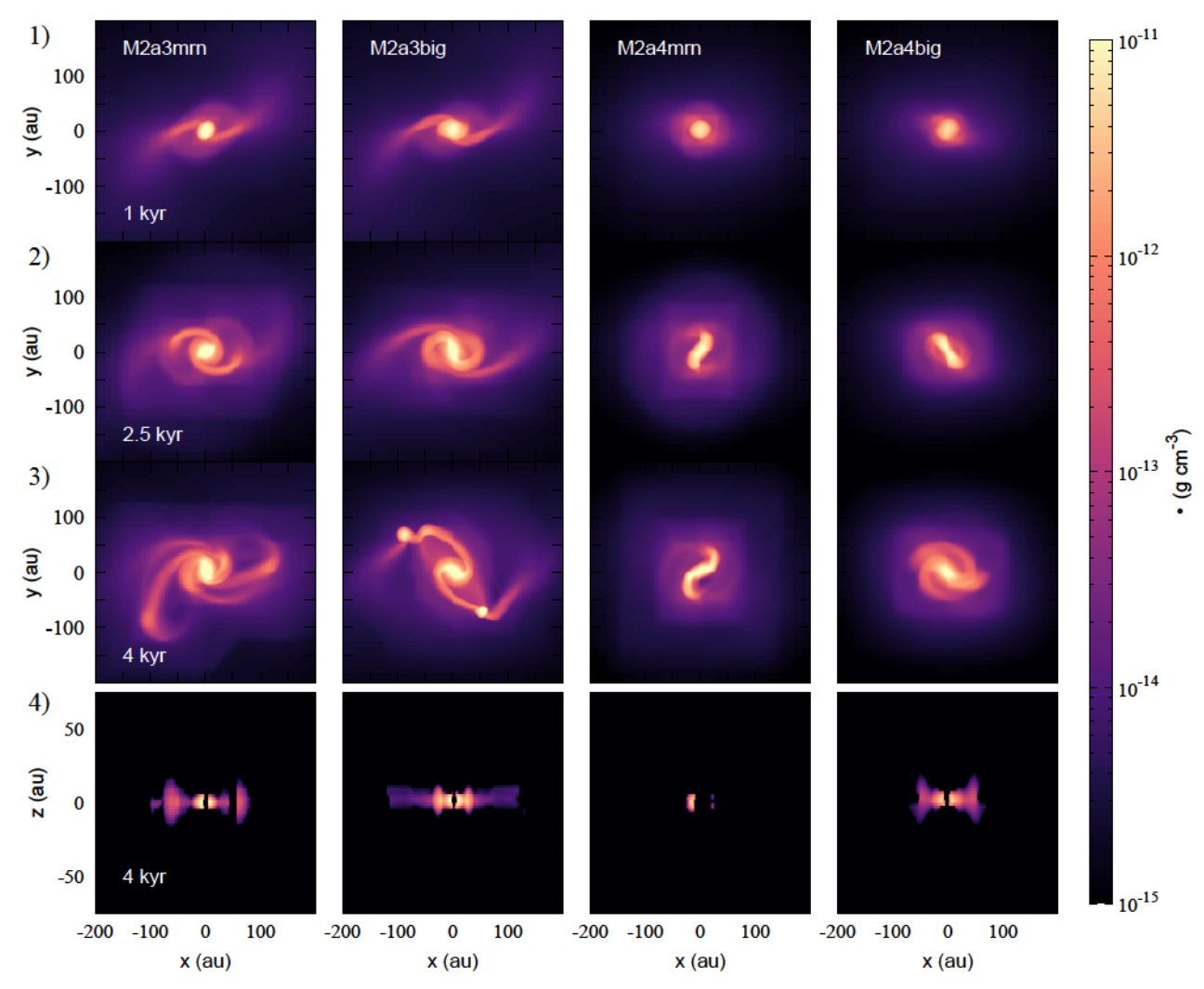


Figure 2. Density maps of the four M=2  $M_{\odot}$  simulations at  $t=t_{\rm C}+1$  kyr (row 1), 2.5 kyr (row 2 and 4) and 4 kyr (row 3). Rows 1 to 3 display slices of the mid-plane, and row 4 shows an edge-on view of the disk at  $t=t_{\rm C}+4$  kyr. In row 4, the gas that does not belong to the disk is not shown.

MRN disks contains however a larger angular momentum (see panel d of figures 4 and 5), meaning that this difference is not significant compared to the influence of the ambipolar diffusion in the outer parts of the disk and in the envelope, although with a higher Elsasser coefficient.

## 3.2. Outflows

All simulations produce bipolar outflows that start within 1 kyr after the first core formation. Figure 7 shows density maps in the outflow region at  $t-t_{\rm C}=2.5$  kyr. The outflows have similar heart-like structures. It appears that the truncated MRN cases produce outflows with an overall slower expansion and a lower density of a factor  $\sim 20$  in the cavity ( $\approx 5 \times 10^{-17}$  g cm<sup>-3</sup> vs

 $\approx 2 \times 10^{-18}~{\rm g~cm^{-3}})$  than the standard distribution. They show a clear cavity with dense borders, while cavity only starts to form at 2.5 kyr with the MRN distribution. The weakness of the truncated MRN outflows are further confirmed when looking at their specific AM and their mass, as shown in Figure 8. With the truncated MRN distribution, the specific AM is 25% to 33% lower than with the standard MRN. In addition, the bottom panel of the figure shows that outflows of the truncated MRN distribution eject significantly less gas. While the mass outflow rate is  $\approx 10^{-5}~{\rm M}_{\odot}~{\rm yr}^{-1}$  for the normal MRN with  $\alpha=0.3$ , and  $\approx 6\times 10^{-6}~{\rm M}_{\odot}~{\rm yr}^{-1}$  with  $\alpha=0,4$ , all four truncated MRN cases have mass loss rates  $\lesssim 2.5\times 10^{-6}~{\rm M}_{\odot}~{\rm yr}^{-1}$ .

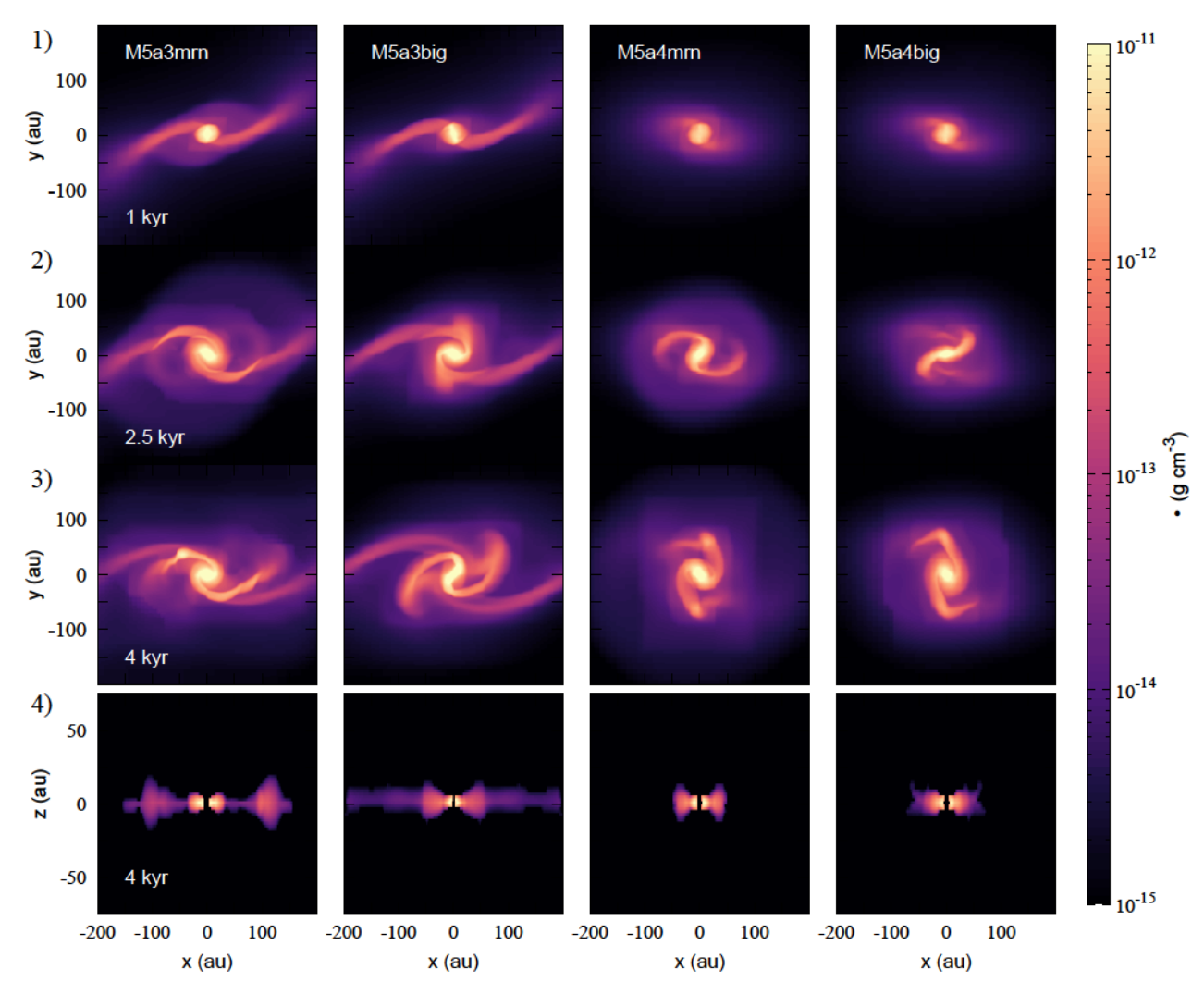
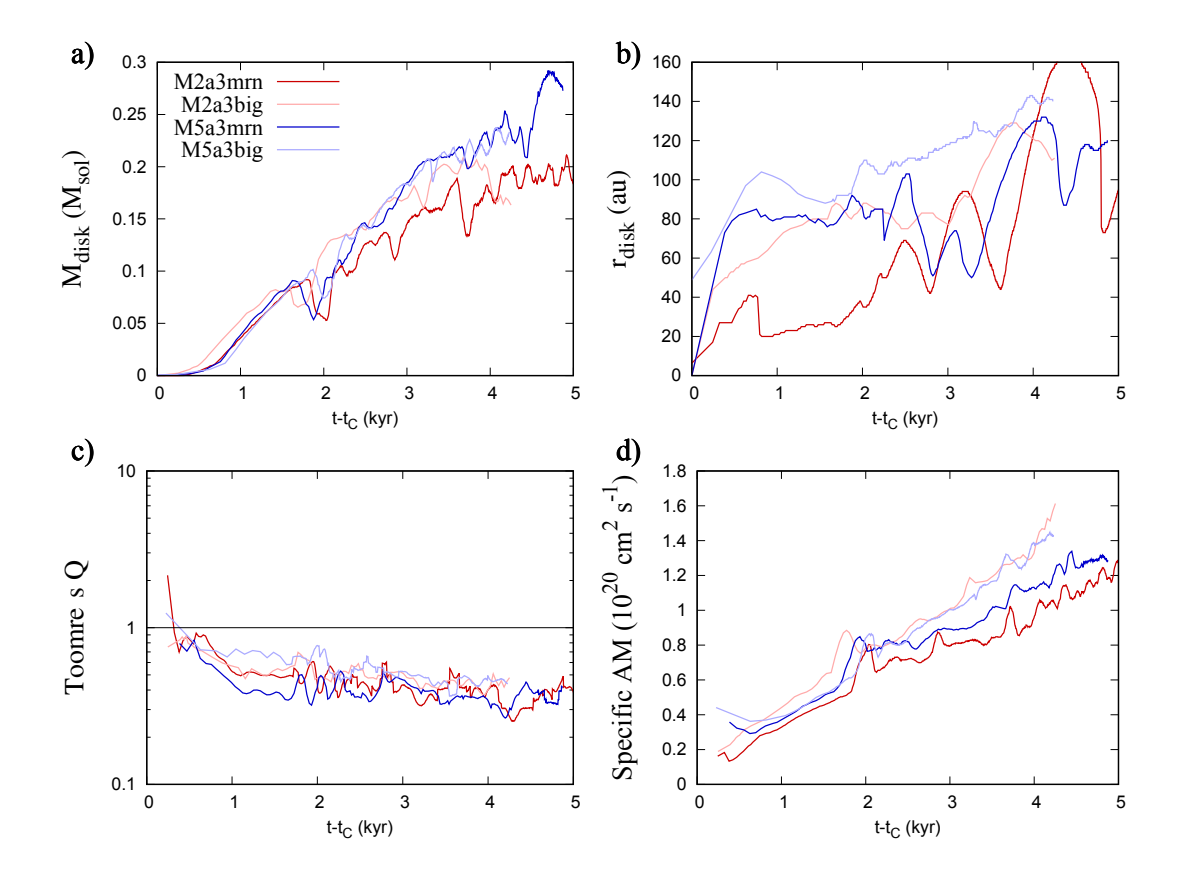


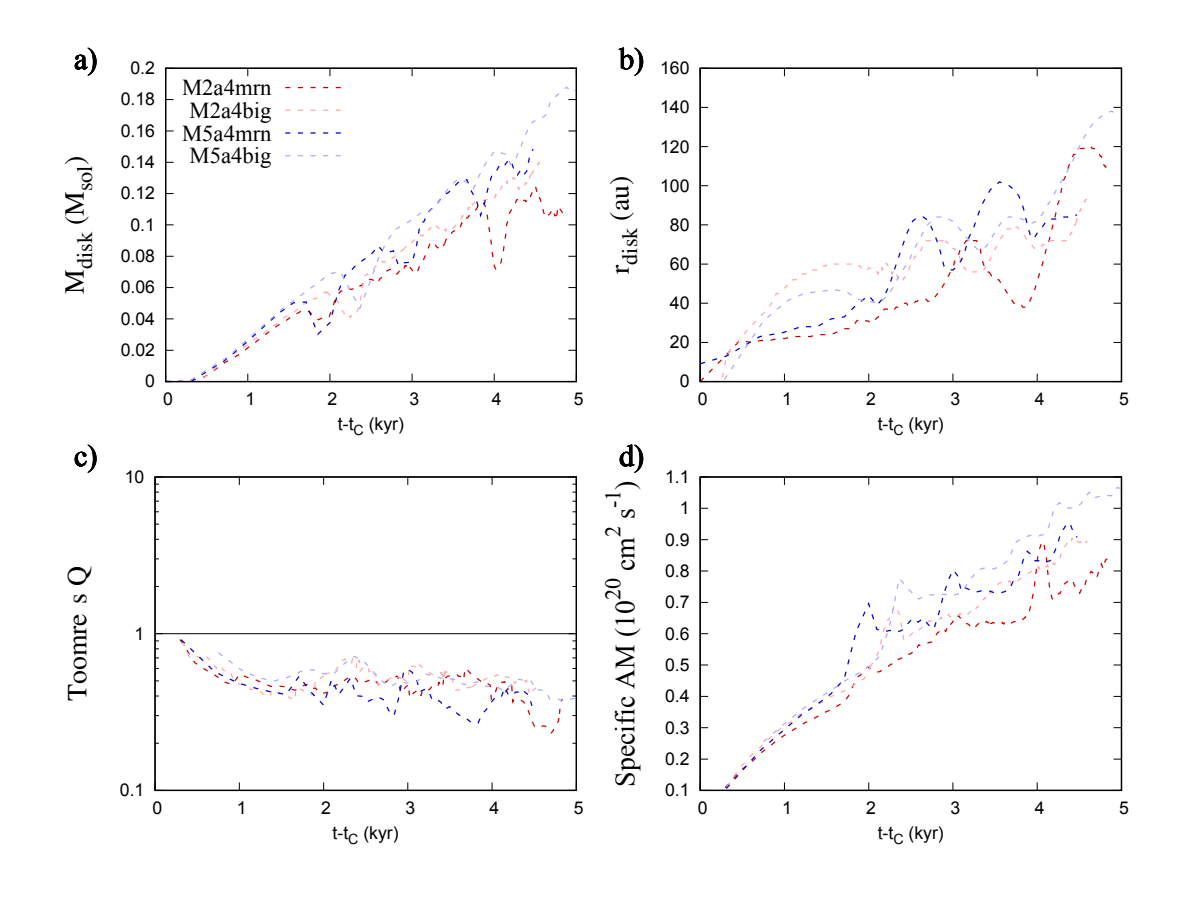
Figure 3. Same as Figure 2 for  $M=5~M_{\odot}$ 

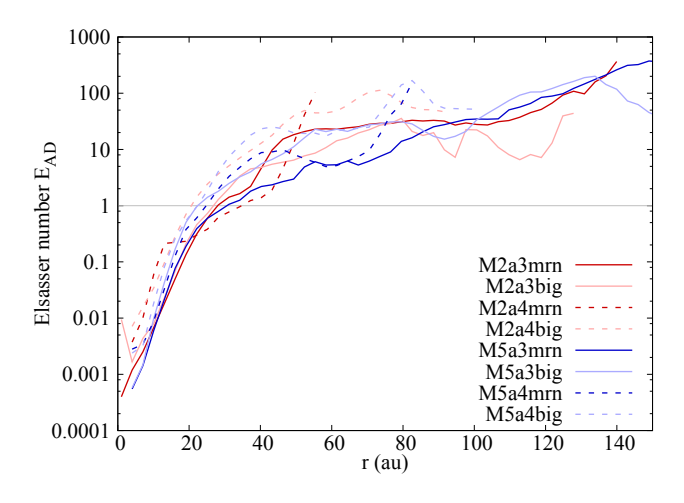
The cases with  $\alpha=0.4$  also eject less AM for the normal distribution, but a similar amount than  $\alpha=0.3$  with the truncated MRN. However these quantities do not depend on the dense core's mass. These observations remain qualitatively unaltered if considering the specific AM instead.

In our simulations, the outflows are launched by Blandford & Payne (1982) mechanism. The magnetic field lines are bent by the drag of the collapsing gas, producing the well-known hourglass-shape. If the angle is high enough, the centrifugal acceleration added to the Lorentz force may eject the gas along the field lines. In the default MRN cases, the field lines can be bent up to an angle of 75° with the z-axis near the central region, which is a 15° slope for the gas acceleration in the outward radial-direction. However, with the truncated MRN, the higher ambipolar coefficient in the en-

velope reduces the accretion of the magnetic field due to a weaker coupling with the gas, resulting in a maximum angle of 65°. These inclination angles of the magnetic field, calculated as  $atan(B_r/B_z)$ , are displayed in Figure 9 for both M5a3mrn and M5a3big simulations, 2.5 kyr after the formation of the first Larson core, in the plane x = 0. The pseudo-disk and the contour of the outflow appear clearly. Figure 9 also include maps of  $B_{\phi}/B_z$ , which shows that the relative strength of  $B_{\phi}$  is overall higher with the truncated distribution. We discuss this point more in details in Section 3.4. Another consequence of the decoupling is the reduced magnetic field strength with the truncated distribution, twice as low as with the default distribution in the vicinity of the outflow launching region. Both these effects reduce the magneto-rotational acceleration of the gas. However, while it is difficult to accurately measure the opening







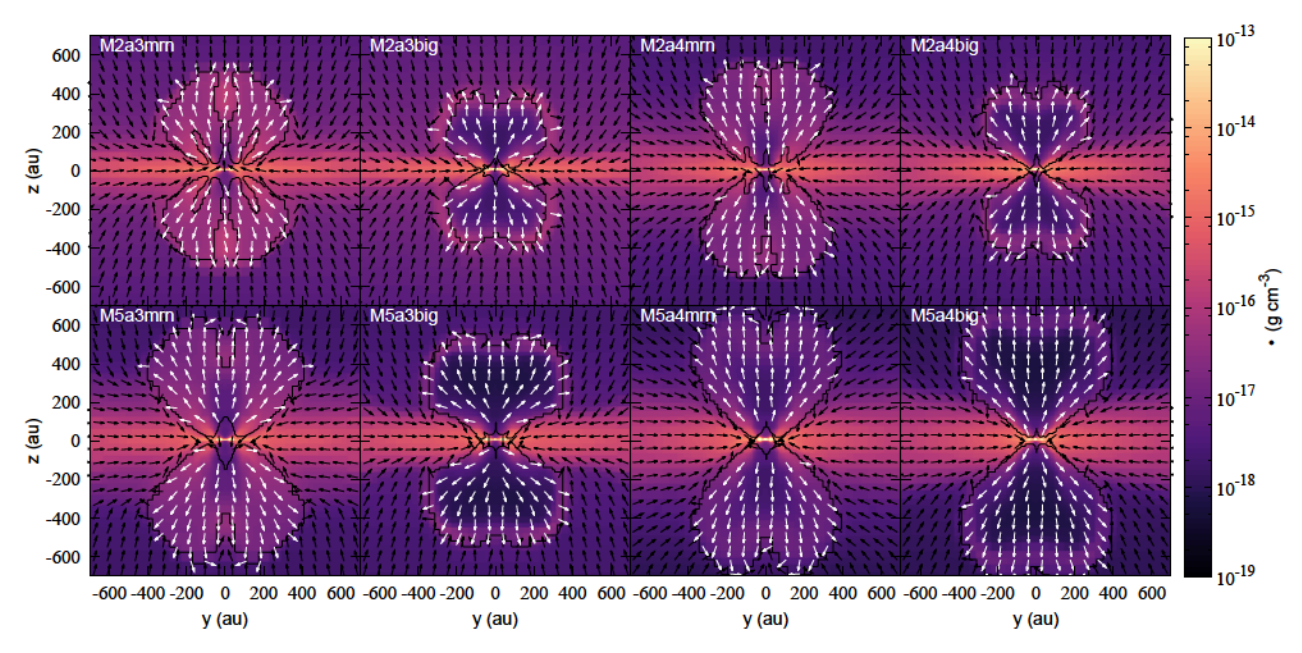


Figure 7. Density slices along the plane x=0 for all simulations at  $t = t_{\rm C} + 2.5$  kyr. The black lines represent the contour of the outflows and arrows indicate the fluid velocity. Infalling material is marked with black arrows while the outflow is marked with white arrows. Top: M=2  $M_{\odot}$ , bottom: M=5  $M_{\odot}$ . From left to right: M\*a3mrn, M\*a3big, M\*a4mrn, M\*a4big.

ambipolar diffusion dominates. We observe the opposite phenomenon outside the disk. While the larger  $\alpha$  decreases the magnetic torque by one order of magnitude, the grain size-distribution does not alter it. However, we probe here only the mid-plane of the pseudo-disk, in which the ambipolar resistivity is low in both cases. Most of the magnetic braking would take place in outer layers.

Figure 12 compares the disk and pseudo-disk AM with the amount extracted by magnetic braking, as well as with the AM taken away by the outflow. Panel a) shows that the magnetic braking has removed three to four times (at  $t = t_C + 5$  kyr) the AM left in the disk, meaning that only 20 to 25 percent of the accreted AM remains in the disk. The magnetic braking is more efficient in the disk for the truncated MRN simulations, which is consistent with a slightly lower ambipolar diffusion coefficient (see Fig. 1). However, panel b) shows that the magnetic braking is the most active in the pseudodisk. With the MRN distribution, more AM is removed by magnetic braking in the pseudo-disk (up to a factor 3 at  $t = t_{\rm C} + 5$  kyr). With the truncated distribution, the magnetic braking is similar in both region. The pseudo-disk is therefore of prime importance when considering the magnetic braking. This is also demonstrated by panel c), which shows the ratio of magnetic braking and AM for the disk and the pseudo-disk combined. Only 10 to 14 percent of the AM remains in this structure for the MRN distribution, and 16 to 25 percent for the truncated MRN cases. The magnetic braking is stronger in the lower-mass cores of  $M=2~{\rm M}_{\odot}$  simulations than in  $M=5~{\rm M}_{\odot}$  simulations. Conversely, the  $\alpha$  parameter does not change sensitively the amount of AM removed by magnetic braking. Panel d) displays the ratio between the AM taken away by the outflow and the magnetic braking. The magnetic braking largely dominates the outflow by a factor of two to ten with the MRN distribution, and ten to a hundred with the truncated MRN. In this latter case, both the magnetic braking and outflows remove significantly less AM than in the MRN distribution, which further confirms the results of Zhao et al. (2016). Panel e) presents the ratio of escaped AM (MB in the disk and pseudo-disk + outflow) to the accreted AM (that comprises the AM of the disk, the pseudo-disk, the outflow and the amount of AM removed by MB in the disk+pseudo-disk) (See Figure 11 for a schematic view of the different considered AM). It shows that 80-90% of the accreted angular momentum escapes by the outflow or the MB. Panel f) shows the ratio between the AM of the disk and the accreted AM. This ratio remains constant at about 10% throughout the life first Larson core, complementary to the  $\approx 90\%$ ratio of the escaped AM. Panels g), h) and i) show the accreted AM, the escaped AM and the AM of the disk compared to the total AM of the core. By  $t = t_{\rm C} + 4$ kyr, 0.1% to 3% of the total AM has made its way and

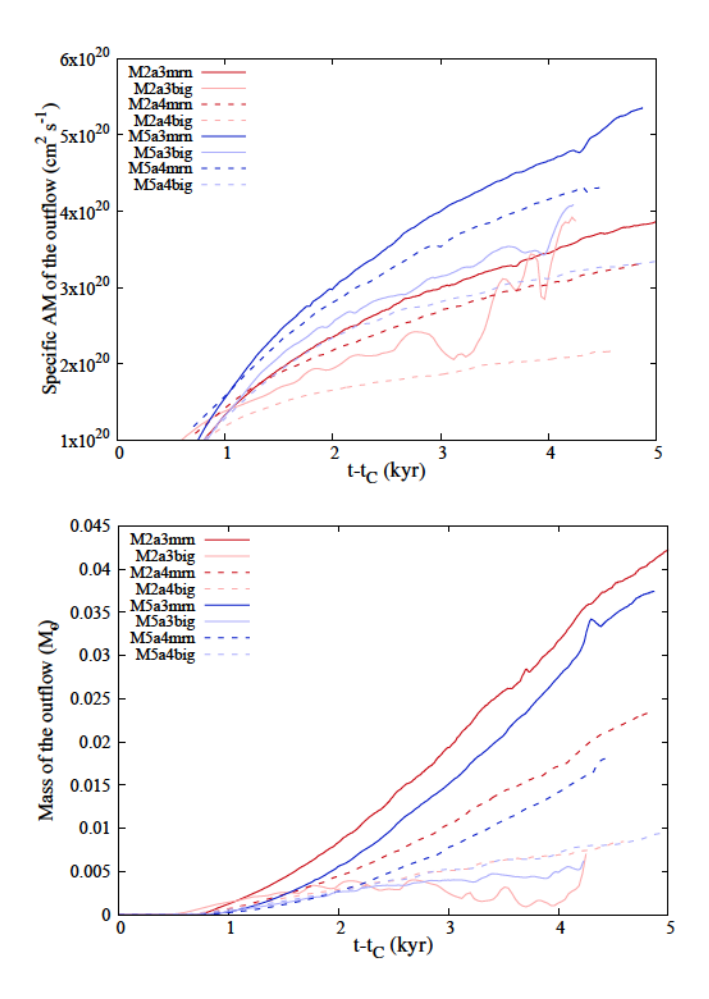


Figure 8. Time evolution of the specific AM (top panel) and the mass (bottom panel)

of the outflow. The curves are the same as in Figure 4 and 5.

stayed into the disk, concentrated in 5-10% of the total mass. As expected, the ratio is systematically larger for the truncated MRN cases. Panel h) indicates that 1% to 30% of the total AM have been removed by MB or the outflow by  $t=t_{\rm C}=4$  kyr, this amount being larger for the normal MRN. All the  $2~{\rm M}_{\odot}$  clouds have accreted a larger fraction of their total AM than the  $5~{\rm M}_{\odot}$  cases, and thus concentrate a larger fraction of the total AM into their disk, whilst experiencing a larger loss of AM.

## 3.3.2. AM in the outflow

Figure 13 shows a slice at the outflow scale of the specific AM, for M5a3mrn. Most of the specific AM of the outflow is located in the bottom wall of the cavity, with values larger than  $10^{21}$  cm<sup>2</sup> s<sup>-1</sup>. This area seems connected to the outer layer of the pseudo-disk, that contains a similar specific AM, higher than in the

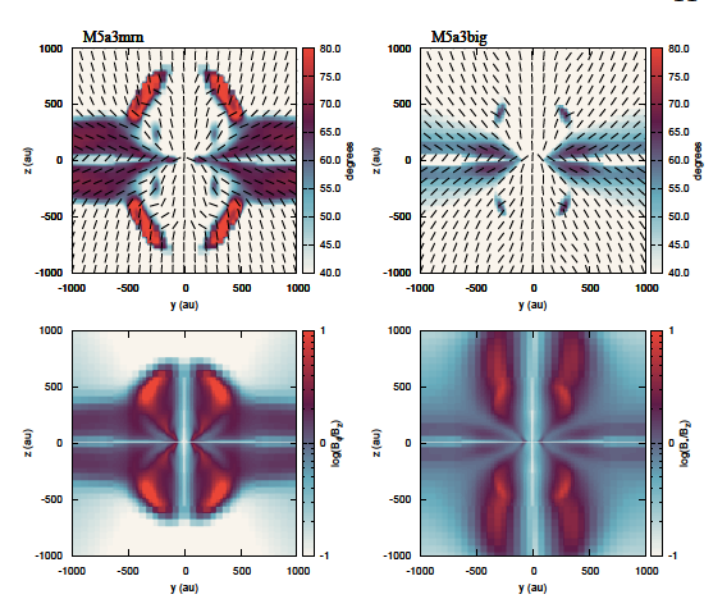


Figure 9. Top panels: Angle between the local magnetic field and the initial magnetic field (vertical) in the y-z plane, at  $t=t_{\rm C}+2.5$  kyr, calculated as  ${\rm atan}(B_r/B_z)$ . The segments represent the direction of the magnetic field. Bottom panels:  $\log(B_\phi/B_z)$ . Left column is M5a3mrn and right column is M5a3big.

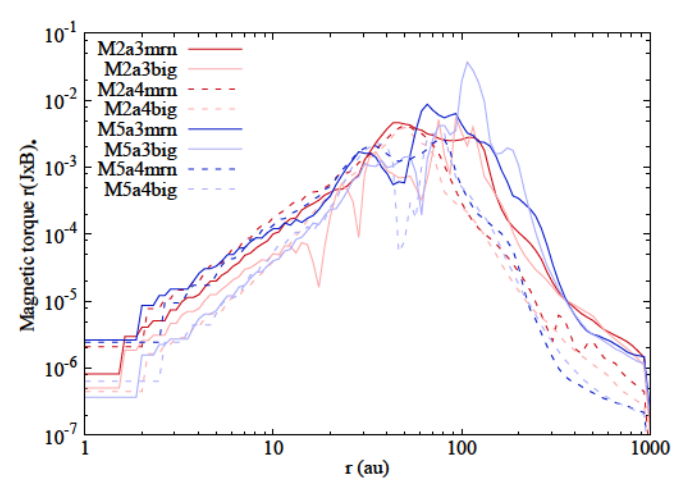
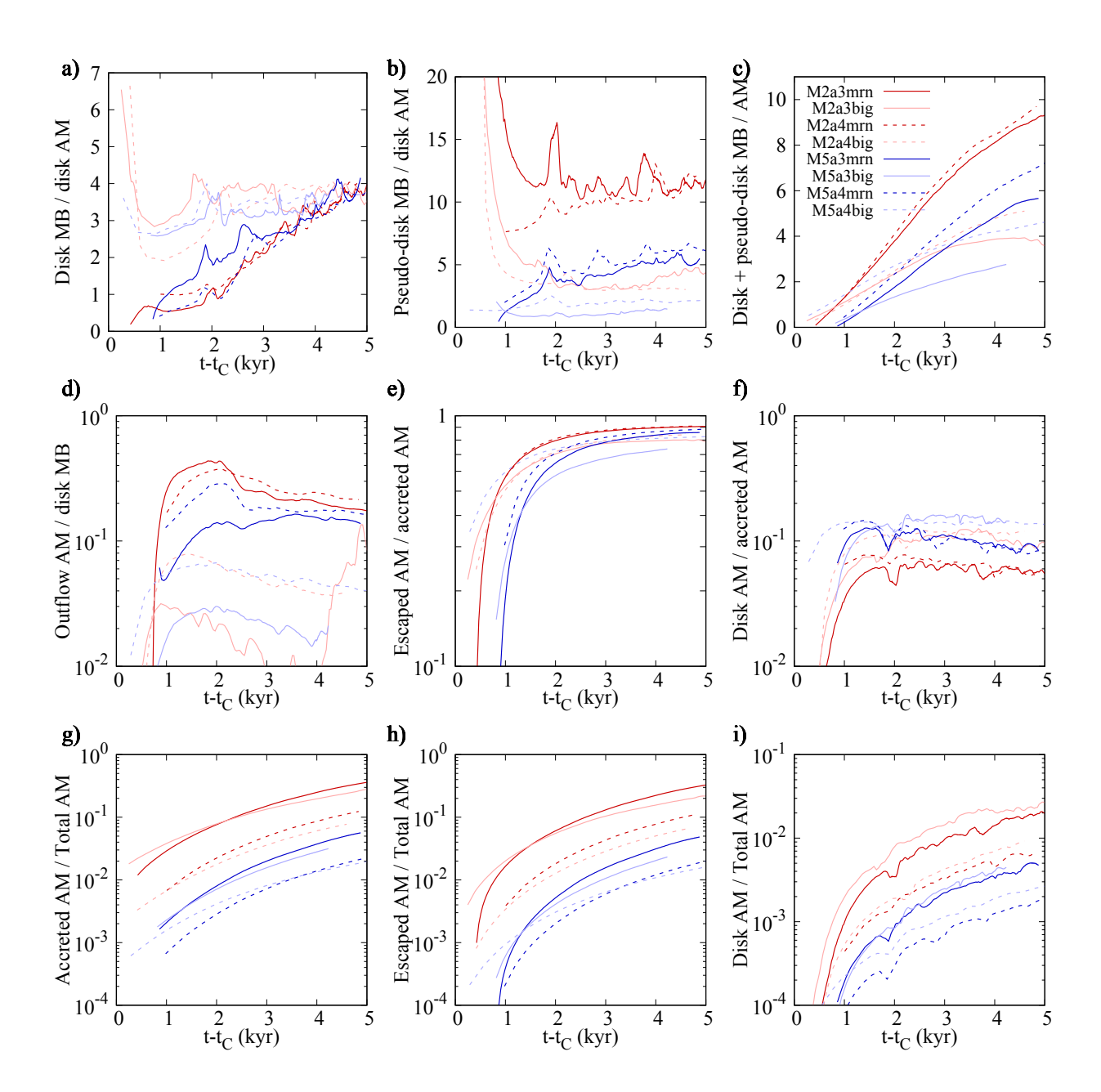


Figure 10. Azimuthal average of the magnetic torque  $r(\mathbf{J} \times \mathbf{B})_{\varphi}$  in the mid-plane as a function of the cylindrical radius.

mid-plane at the same cylindrical radius. We have also plotted the projected trajectories of 75 virtual tracer particles, in thin black and white lines. The 50 black particles are randomly generated in the outflow in the final time-step, and the 25 white particles are are generated only in the high specific AM region. In post-processing calculations, we have integrated the particles trajectory backwards using the local flow velocity. This

## Total AM Accreted AM Escaped AM outflow AM pseudo-disk MB, disk MB pseudo-disk AM, disk AM



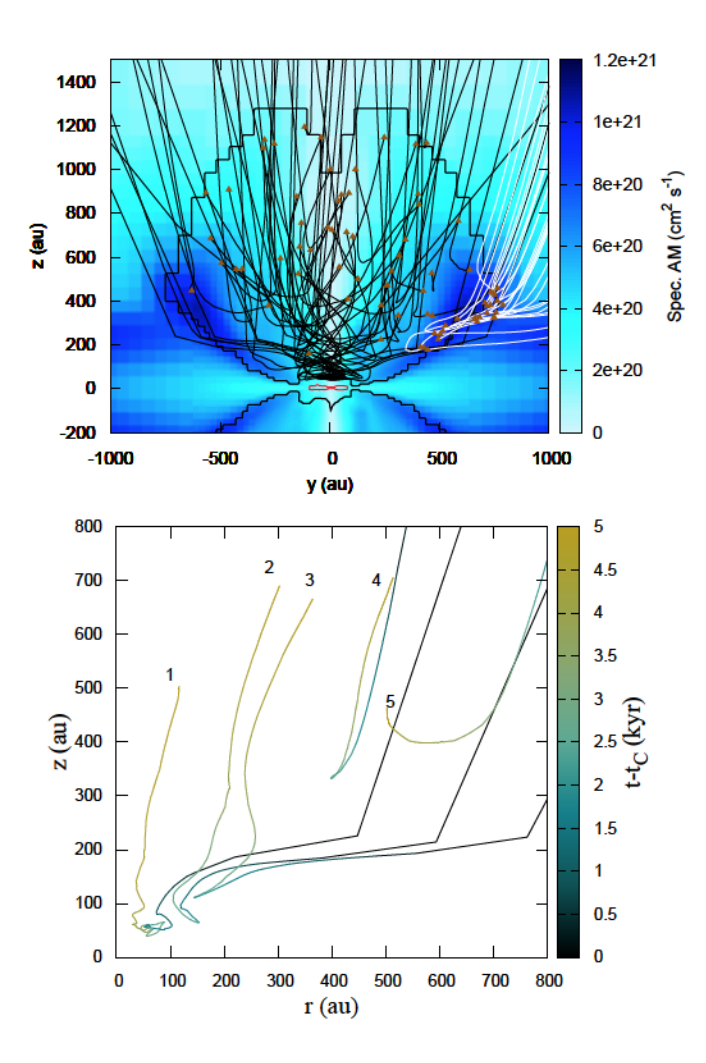


Figure 13. Specific AM of the gas in the outflow region in the plane x=0, for M5a3mrn. The thicker black line represent the boundaries of the outflow at  $t-t_{\rm C}=5$  kyr. Thin lines are the trajectories, projected onto the yz-plane, of virtual tracer particles located in the outflow in the last output, and whose path is integrated backward in time. The 50 black particles are randomly distributed in the outflow, and the 25 white particles are distributed only in the region of high specific AM. The brown triangles indicate the location of the particles in the last output. For clarity, the abscissa of white trajectories represent the cylindrical radius and not the actual y-coordinate. The red countour represents the disk. The bottom panel shows the r/z trajectory of 5 selected particles, labeled 1 to 5. The color represents the time.

respectively. Inside the pseudo-disk, the drift velocity is negligible, indicating a strong coupling, similarly to the velocity profiles in Figure 14 beyond few 100 au. In the infalling envelope however, the ions weakly decouple as they approach the mid-plane, until they enter the pseudo-disk. For  $|z| \lesssim 500$  au, their trajectory is more bent toward the center than the neutrals. The decou

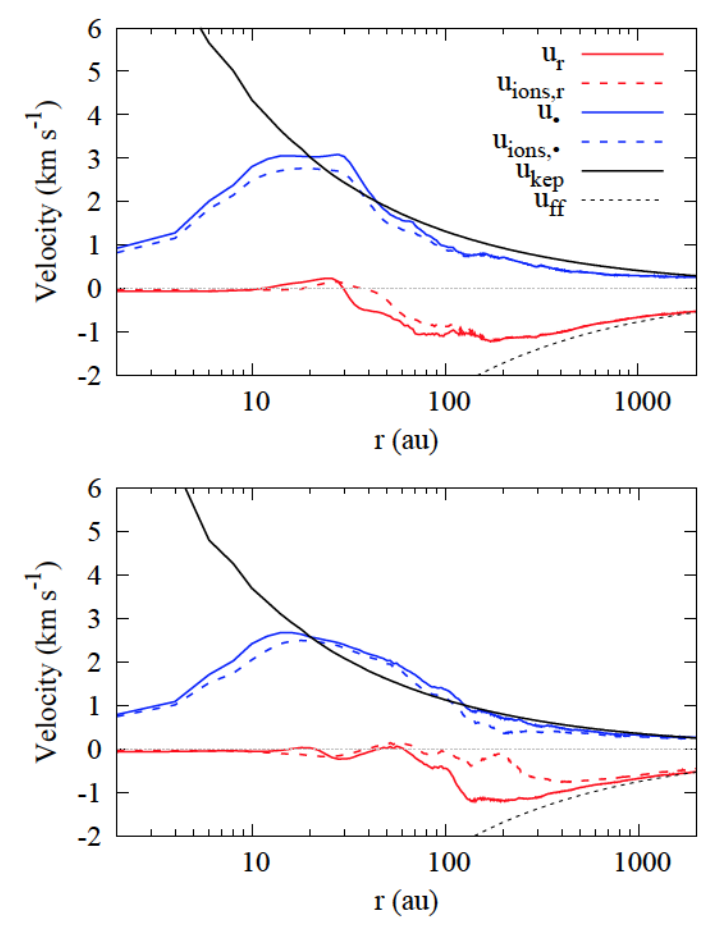
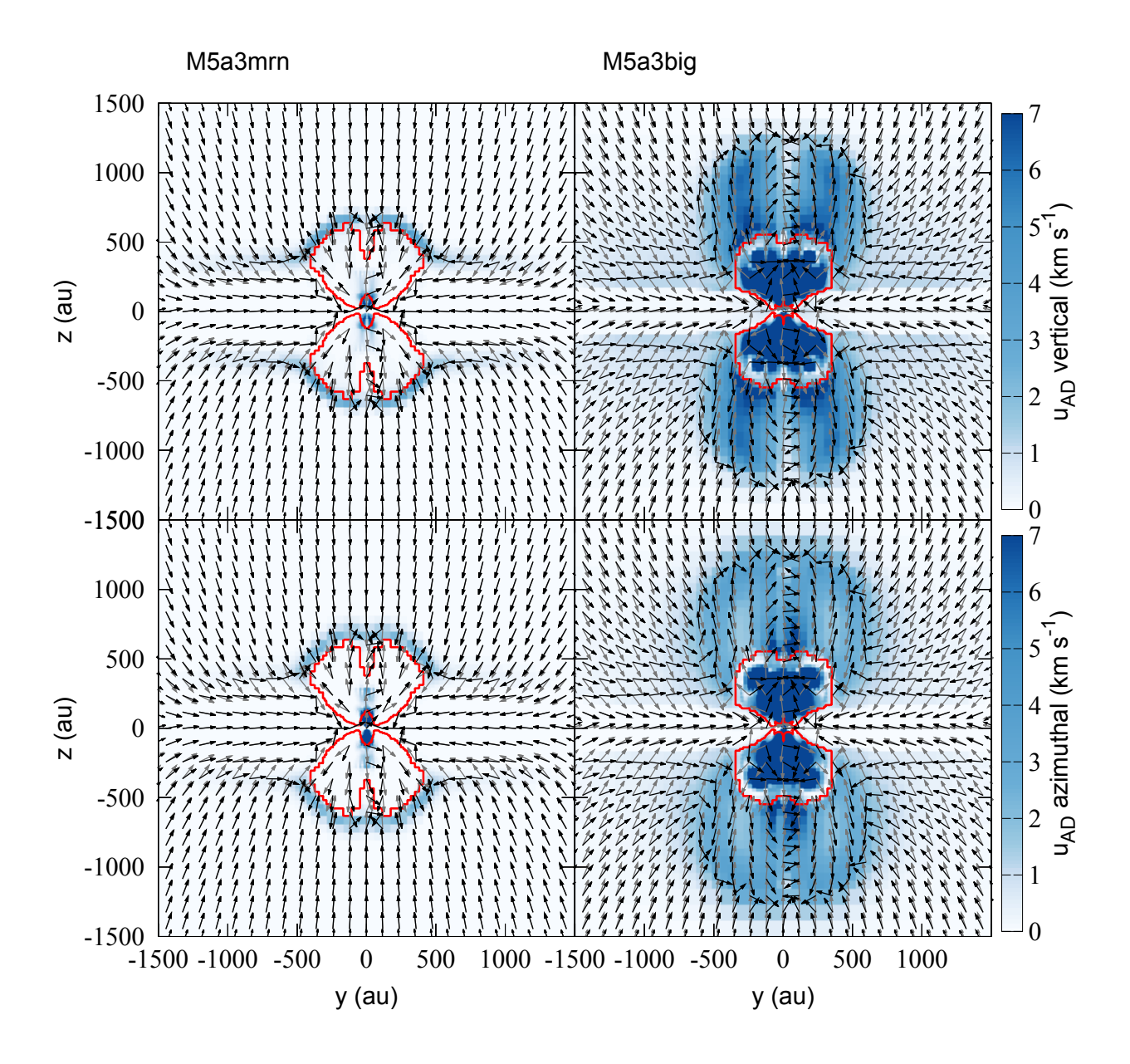


Figure 14. Azimuthaly averaged velocity profiles in the mid-plane for M5a3mrn (top panel) and M5a3big (bottom panel) at  $t-t_{\rm c}=4$  kyr. Red curves represent the radial velocities, blue curves are the azimuthal velocities and the black curve indicate the Keplerian velocity. Solid lines represent the gas while dashed lines represent the ions.

pling is almost negligible in the envelope for the normal MRN distribution, but with the truncated distribution, the drift velocity reads amplitudes  $\gtrsim 1 \text{ km s}^{-1}$ . In the outflow of M5a3big, the drift velocity reaches several  $10 \text{ km s}^{-1}$ , similar to the value of the Alfven velocity, due to the extremely high ambipolar coefficient (two to four orders of magnitude higher than in the envelope or the disk). However, the most striking features are the large zones of strong decoupling in the vicinity of the outflow for the truncated MRN case. Due to the high ambipolar diffusion, caused by the low density, and the strong electric current and magnetic field close to the central axis, the ions drift from the neutrals at velocities of several km  $s^{-1}$ . We even observe an outflow of ions outside and bigger than the actual previouslydescribed outflow. Ions are escaping against the flow of infalling neutrals from the envelope at velocities of sev-



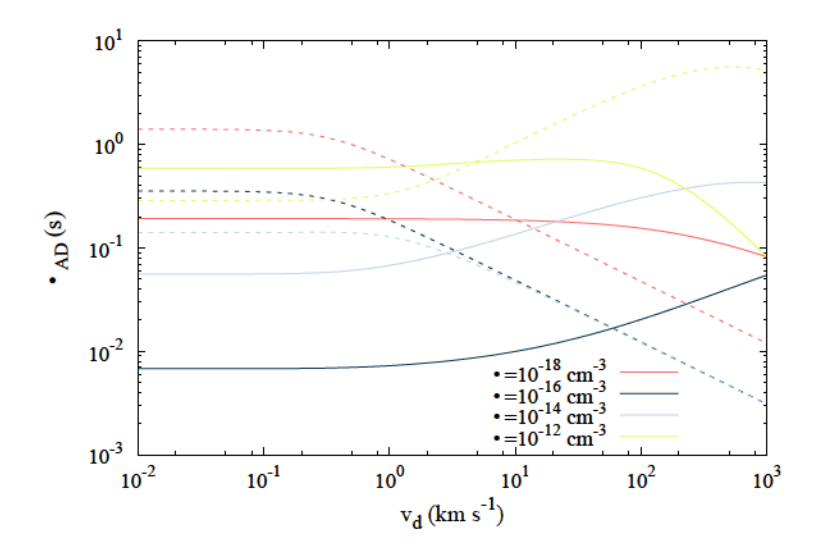


Figure 16. Ambipolar resistivity as a function of  $v_{\rm d}$  for various densities. Red color:  $\rho = 10^{-18}$  g cm<sup>-3</sup>, blue color:  $\rho = 10^{-16}$  g cm<sup>-3</sup>, purple color:  $\rho = 10^{-14}$  g cm<sup>-3</sup>, green color:  $\rho = 10^{-12}$  g cm<sup>-3</sup>. The solid lines represent the MRN case and the dashed lines represent the truncated MRN case.

Bate, M. R. 2018, MNRAS, 475, 5618, doi: 10.1093/mnras/sty169

Belloche, A. 2013, in EAS Publications Series, Vol. 62, EAS Publications Series, ed. P. Hennebelle & C. Charbonnel, 25–66, doi: 10.1051/eas/1362002

Bhandare, A., Kuiper, R., Henning, T., et al. 2018, ArXiv e-prints. https://arxiv.org/abs/1807.06597

Blaes, O. M., & Balbus, S. A. 1994, ApJ, 421, 163, doi: 10.1086/173634

Blandford, R. D., & Payne, D. G. 1982, MNRAS, 199, 883, doi: 10.1093/mnras/199.4.883

Bodenheimer, P. 1995, ARA&A, 33, 199, doi: 10.1146/annurev.aa.33.090195.001215

Bonnor, W. B. 1956, MNRAS, 116, 351

Bontemps, S., Andre, P., Terebey, S., & Cabrit, S. 1996, A&A, 311, 858

Boss, A. P., & Bodenheimer, P. 1979, ApJ, 234, 289, doi: 10.1086/157497

Cabrit, S., & Bertout, C. 1992, A&A, 261, 274

Cardelli, J. A., Clayton, G. C., & Mathis, J. S. 1989, ApJ, 345, 245, doi: 10.1086/167900

Chokshi, A., Tielens, A. G. G. M., & Hollenbach, D. 1993, ApJ, 407, 806, doi: 10.1086/172562

Crutcher, R. M. 1999, ApJ, 520, 706, doi: 10.1086/307483

Desch, S. J., & Turner, N. J. 2015, ApJ, 811, 156, doi: 10.1088/0004-637X/811/2/156

Draine, B. T. 2011, Physics of the Interstellar and Intergalactic Medium

Draine, B. T., & Sutin, B. 1987, ApJ, 320, 803, doi: 10.1086/165596 Duffin, D. F., & Pudritz, R. E. 2008, MNRAS, 391, 1659, doi: 10.1111/j.1365-2966.2008.14026.x

Dzyurkevich, N., Commerçon, B., Lesaffre, P., & Semenov,
 D. 2017, A&A, 603, A105,
 doi: 10.1051/0004-6361/201628995

Ebert, R. 1955, Zeitschrift fr Astrophysik, 37, 217

Ferreira, J., Dougados, C., & Cabrit, S. 2006, A&A, 453, 785, doi: 10.1051/0004-6361:20054231

Fromang, S., Hennebelle, P., & Teyssier, R. 2006, A&A, 457, 371, doi: 10.1051/0004-6361:20065371

Galli, D., Lizano, S., Shu, F. H., & Allen, A. 2006, ApJ, 647, 374, doi: 10.1086/505257

Gillis, J., Mestel, L., & Paris, R. B. 1974, Ap&SS, 27, 167, doi: 10.1007/BF00641596

Goodman, A. A., Benson, P. J., Fuller, G. A., & Myers, P. C. 1993, ApJ, 406, 528, doi: 10.1086/172465

Guillet, V., Hennebelle, P., Marcowith, A., et al. submitted Harten, A., Lax, P., & Van Leer, B. 1983, SIAM Review, 25, 35, doi: 10.1137/1025002

Hennebelle, P., Commerçon, B., Lee, Y.-N., & Charnoz, S. 2020, A&A, 635, A67, doi: 10.1051/0004-6361/201936714

Hennebelle, P., & Fromang, S. 2008, A&A, 477, 9, doi: 10.1051/0004-6361:20078309

Higuchi, K., Machida, M. N., & Susa, H. 2019, MNRAS, 486, 3741, doi: 10.1093/mnras/stz1079

Hocuk, S., & Cazaux, S. 2015, A&A, 576, A49, doi: 10.1051/0004-6361/201424503

Joos, M., Hennebelle, P., & Ciardi, A. 2012, A&A, 543, A128, doi: 10.1051/0004-6361/201118730